

OPEN

Photocatalytic Degradation of Organic Pollutants over MFe_2O_4 ($M = Co, Ni, Cu, Zn$) Nanoparticles at Neutral pH

Nishesh Kumar Gupta^{1,2}, Yasaman Ghaffari^{1,2}, Suho Kim^{1,2}, Jiyeol Bae², Kwang Soo Kim^{1,2*} & Md Saifuddin^{1,2}

In this study, we report a surfactant-mediated synthesis of ferrites (MFe_2O_4 ; $M = Co, Ni, Cu, Zn$) using the co-precipitation-oxidation method. The band gap calculated from UV-Visible diffuse reflectance spectra were found in the range of 1.11–1.81 eV. These ferrite nanocatalysts were studied for the photocatalytic degradation of multiple organic dyes in a 32W UV-C/ H_2O_2 system. All the four ferrites showed an excellent dye degradation rate in the range of 2.065–2.417 min^{-1} at neutral pH. In the optimized condition, NiF was found to degrade 89%, 92%, 93%, and 78% of methylene blue, methyl orange, bromo green, and methyl red, respectively within 1 min of UV-irradiation. A 40% TOC removal was recorded after 5 min of degradation reaction, which increased to 60% after 50 min. Mechanism elucidated by scavenger studies and fluorescence spectroscopy revealed that $\bullet OH$ and holes were the primary reactive radicals responsible for the degradation process. Ferrite photocatalysts showed an insignificant performance loss in seven consecutive cycles. The photocatalyst was found efficient in the presence of a high concentration of salts. Thus, it was concluded that these photocatalysts are highly suitable for the remediation of dye-contaminated wastewater.

The ever-increasing population, coupled with rapid urbanization and industrialization, have deteriorated the quality of life. Excessive contamination of water bodies could be a severe threat to both human beings and other life forms. Organic dyes are considered as one of the major pollutants discharged into the environment by textile, printing, food, and leather industries¹. Though a large segment of these synthetic dyes is non-toxic or less toxic, their presence in water increases the oxygen demand, which in turn affects aquatic animals². Among the dyes consumed in industries, up to 70% belong to azo dye family (those with azo-functional group “ $-N=N-$ ”). Azo dyes have genotoxic, mutagenic, and carcinogenic effects on living beings³. Some of the azo dyes are known to be carcinogenic in the non-cleaved state, and for many of the azo dyes, their cleaved products such as benzidine are known to induce tumors⁴. Conventional biological, chemical, and physical methods like adsorption^{5,6}, chemical precipitation⁷, and microbial degradation⁸ have been established for the remediation of dye-contaminated wastewater. The practical application of these processes suffers due to high operational cost, sludge production, or formation of secondary pollutants. For a complete or partial degradation of organic dyes (into non-toxic byproducts), degradation by adopting the photocatalytic process is one of the viable options.

In recent years, advanced oxidation processes based on the generation of highly reactive hydroxyl radicals have gained momentum for the degradation of toxic organic pollutants⁹. Though the Fenton process is easier to operate, it suffers badly due to a slow regeneration of Fe^{2+} ions¹⁰. Thus, the ultraviolet radiation or electrochemical method is generally coupled with the Fenton process for the regeneration of Fe^{2+} ions^{10,11}. Unfortunately, the homogeneous photo-Fenton process has two significant drawbacks, i.e., a narrow operational pH range and formation of sludge, which increase the overall cost of the process¹². These drawbacks are motivating researchers to develop cost-effective UV-light responsive heterogeneous photocatalysts.

Among numerous metal-oxide based photocatalysts developed, researchers are fixated on spinel ferrites due to their narrow band gap, magnetic property, and high stability¹³. Moreover, the magnetic and optical properties

¹University of Science and Technology (UST), Daejeon, Republic of Korea. ²Department of Land, Water, and Environment Research, Korea Institute of Civil Engineering and Building Technology (KICT), Goyang, Republic of Korea. *email: kskim@kict.re.kr

of Fe_3O_4 (simplest ferrite) could be easily tuned by replacing Fe^{2+} ions with other divalent cations (Mn, Co, Ni, Cu, Zn, Ca, and Mg)¹⁴. Many researchers have exploited ferrite photocatalysts for the photocatalytic degradation of organic pollutants. Cai *et al.*, 2016 developed ZnFe_2O_4 via a reduction-oxidation method, which showed decolorization of Orange II dye in visible light/catalyst/ H_2O_2 system¹⁵. Sharma *et al.*, 2014 synthesized MFe_2O_4 (M = Co, Ni, Cu, Zn) by sol-gel method and studied the degradation of methylene blue at pH 2.5 in visible light/catalyst/ H_2O_2 system¹⁶. Dhiman *et al.*, 2016 reported visible light-assisted photocatalytic degradation of safranin-O and remazol brilliant yellow at pH 2.5 onto morphologically different NiFe_2O_4 synthesized by hydrothermal route¹⁷. Though these studies showed remarkable visible-light-driven photocatalytic degradation of organic dyes, significant issues with these research works were low pH requirement, slow degradation kinetics, and high energy consumption.

Considering these drawbacks as challenges, we focused on the development of novel ferrite photocatalysts, which could be used for dye degradation at neutral pH with low energy consumption. We successfully developed an economical and robust surfactant-mediated co-precipitation method for the fabrication of spinel ferrites (MFe_2O_4 ; M = Co, Ni, Cu, Zn). The prepared photocatalysts were characterized by various microscopic and spectroscopic techniques for understanding the structural, functional, and optical properties. These ferrite photocatalysts were found highly efficient in degrading multiple organic dyes at neutral pH in a 32 W UV-C/ H_2O_2 system. The kinetic rates observed in the present study were the highest ever reported under these sets of experimental conditions. Furthermore, the dye degradation mechanism was deduced based on the scavenger studies and fluorescence spectroscopy.

Results and discussions

Characterization of ferrite photocatalysts. The morphology of ferrite photocatalysts was characterized by scanning electron microscopy (SEM), and results have been shown in Supplementary Fig. 1. SEM micrographs of all the four photocatalysts, i.e., CoF, NiF, CuF, and ZnF showed a coral-like morphology. EDS analysis of CoF photocatalyst has been shown in Supplementary Fig. 2. From the EDS spectrum in Supplementary Fig. 2(a), Fe, Co, and O were observed at their corresponding keV values. The peaks of Pt observed in the EDS spectrum were due to the coating at the time of SEM analysis for better visibility of the surface morphology. The 2D elemental mappings showed a uniform distribution of constituent elements in CoF, thus confirming the homogeneity of the photocatalyst (Supplementary Fig. 2(b)).

The morphology of ferrites was further investigated by high-resolution transmission electron microscopy (HRTEM). Single crystals were observed for all the four ferrites (Supplementary Fig. 3). The crystallite planes were assigned by measuring the fringe width values on the HRTEM image and then correlating it with the interplanar spacing (d) values from the XRD pattern. The fringe width of 0.48 nm corresponding to the (111) plane was observed for both CoF and NiF ferrites. The same fringe width was also observed for CuF, but it was assigned to the (101) plane of the tetragonal crystal system. For ZnF, the two fringes width, 0.299 nm (220), and 0.162 nm (511) were distinctly visible (Fig. 1).

Porosity properties and specific surface area of ferrite nanoparticles were analyzed by N_2 adsorption-desorption isotherm (Supplementary Fig. 4). All the four ferrites showed a similar hysteresis loop at a high relative pressure fit for type IV of adsorption isotherm corresponding to the mesoporous materials¹⁸. The hysteresis loop at a high relative pressure (P/P_0) in the range of 0.5–1.0 showed that the mesopores are irregular in the photocatalyst which was further confirmed by the Barrett, Joyner, and Halenda pore size distribution (inset images in Supplementary Fig. 4). The three photocatalysts, i.e., CoF, NiF, and CuF, showed a broader pore size in the range of 3–250 nm. In contrast, for ZnF, pore size in the range of 3–60 nm with a narrow peak centered at ~35 nm showed non-uniform sizes and shapes of the nanopores from the agglomeration of ferrite nanoparticles. The method for calculating total surface area (S_{tot}) and BET surface area (S_{BET}) of ferrites nanoparticles has been given in Supplementary Section 1. The S_{BET} for ferrites in the range of 13–23 $\text{m}^2 \text{g}^{-1}$ were found lower than those reported in the literature where ferrites were synthesized by sol-gel method¹⁶. Various parameters like S_{tot} , S_{BET} , pore volume (V_p), and pore diameter (D_p) have been tabulated in Supplementary Table 1.

Figure 2(a) showed the X-ray diffraction (XRD) pattern of CoF, NiF, CuF, and ZnF. The diffraction peaks of CuF nanoparticles at 18.3°, 29.9°, 35.3°, 37.1°, 43.9°, 54.1°, 57.1°, 58.0°, 62.1°, and 64.0° were assigned to (hkl) (101), (112), (103), (211), (202), (220), (312), (303), (321), (224), and (400) planes of tetragonal CuFe_2O_4 (JCPDS card no. 34–0425)¹⁹. The lattice parameters, a (5.83 Å) and c (8.61 Å), matched well with the literature²⁰. Besides, the diffraction peaks appeared for CoF, NiF, and ZnF matched with the JCPDS card no. 22–1086, 10–0325, and 22–1012, respectively. The lattice parameter for these cubic spinel structures, $a = 8.38$ Å (CoF), 8.34 Å (NiF), and 8.45 Å (ZnF), was found consistent with the earlier reported values¹⁶. In NiF and CuF photocatalysts, Fe_2O_3 was confirmed as an impurity that was absent in CoF and ZnF. The crystallite size of a ferrite nanoparticle was calculated using the Debye-Scherrer equation: $D = 0.9\lambda/(\beta \cos\theta)$, where D is the crystallite size, λ is the wavelength of Cu K α radiation, β is the full width at half maximum of the diffraction peak, and θ is the Bragg angle²¹. The crystallite size for CoF, NiF, CuF, and ZnF was found to be 34 nm, 27 nm, 16 nm, and 36 nm, respectively (Supplementary Table 2).

Figure 2(b) showed the Fourier-transform infrared (FTIR) spectra of CoF, NiF, CuF, and ZnF photocatalysts. Two distinct bands for metal-oxygen vibrations were observed in the range of 750–400 cm^{-1} for all the four ferrite photocatalysts. The high-intensity band in the range of 750–500 cm^{-1} (ν_1) was attributed to the intrinsic stretching vibrations of the tetrahedral site-occupied metal-oxygen bond [$\text{M}^{2+}_{\text{tetra}} \leftrightarrow \text{O}$]. The low-intensity band 450–400 cm^{-1} (ν_2) was due to the octahedral Fe^{3+} -oxygen stretching vibration²¹. The broad band centered at 3427 cm^{-1} and a low-intensity band centered at 1630 cm^{-1} were assigned to the stretching and bending mode of O–H bonds of physically adsorbed water molecules.

Ultraviolet visible diffuse reflectance spectroscopy (UV-Vis DRS) analysis was performed to evaluate the optical properties of ferrite photocatalysts, and results have been shown in Fig. 2(c). All four ferrites showed a strong

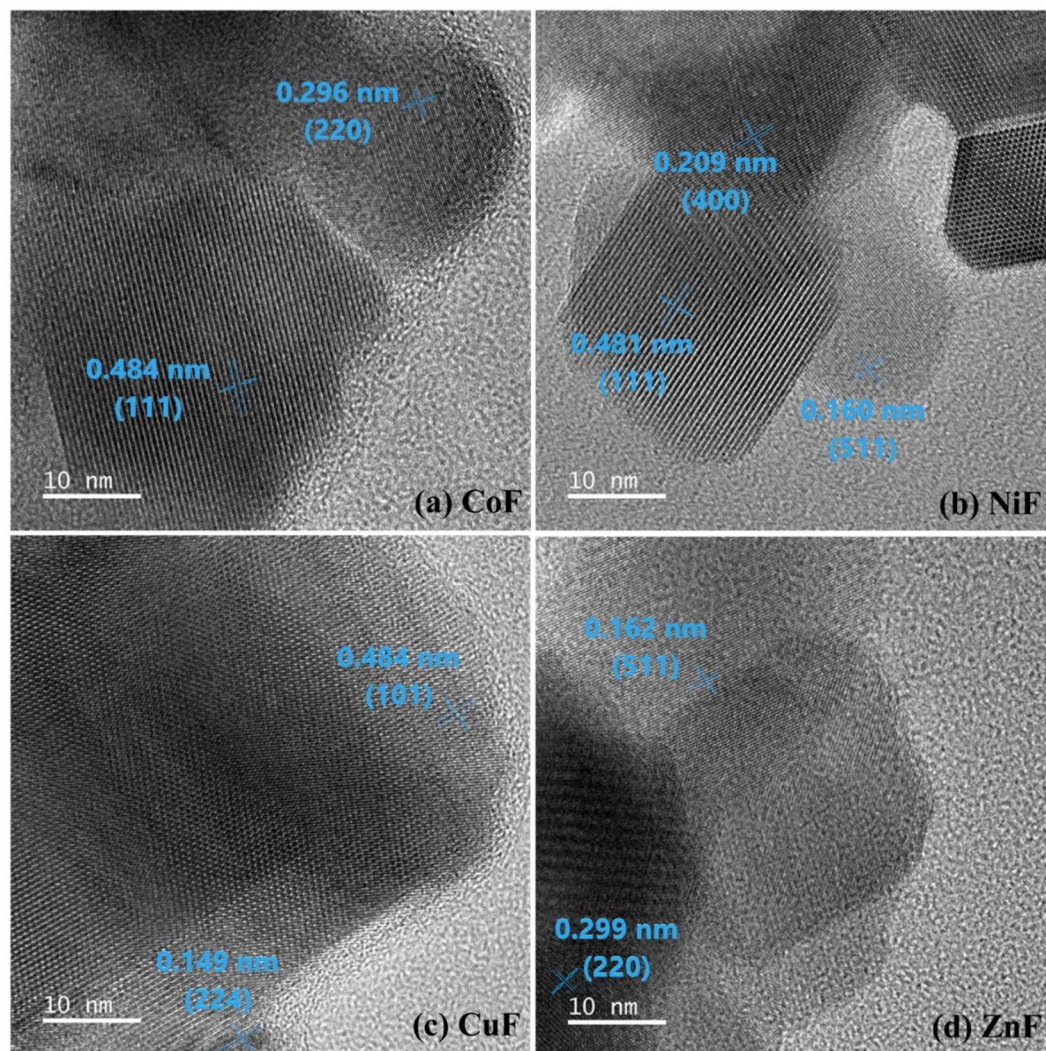


Figure 1. HRTEM images of (a) CoF (b) NiF (c) CuF (d) ZnF photocatalysts.

absorption band in the entire UV-Visible region. The optical direct band gap was calculated using the following equation²²:

$$(\alpha hv)^2 = B(h\nu - E_g) \quad (1)$$

where, α , ν , and B are absorption coefficient, light frequency, and the proportionality constant, respectively. The $(\alpha hv)^2$ versus $h\nu$ plots for ferrite photocatalysts have been shown in Fig. 2(d). The band gap calculated for CoF, NiF, CuF, and ZnF, i.e., 1.11 eV, 1.59 eV, 1.55 eV, and 1.81 eV, respectively, were found significantly lower than those reported in the literature¹⁶.

X-ray photoelectron spectroscopy (XPS) analysis was carried out to determine the elemental composition and oxidation states of ferrite photocatalysts. The XPS full scan spectra of ferrites (Fig. 3(a)) confirmed the existence of predominant constituent elements. The high-resolution XPS (HRXPS) spectra of individual elements have been deconvoluted using Fityk software. In the deconvoluted HRXPS O 1s spectrum (Fig. 3(b)), two peaks at 529.52 eV and 531.67 eV were assigned to the metal-oxygen bonds (lattice oxygen) and oxygen defect sites, respectively²³. The proportion of oxygen defect sites was found significantly higher for CoF photocatalyst (image not shown here). In the HRXPS Fe 2p spectrum (Fig. 3(c)), two spin-orbit doublets Fe 2p_{3/2} (709.47 eV for B-sites and 710.55 eV for A-sites) and Fe 2p_{1/2} (723.67 eV for B-sites and 725.86 eV for A-sites) were observed for Fe³⁺ ions in the ferrite photocatalyst. The peaks at 718.42 eV, 723.67 eV, and 731.87 eV were satellite peaks²⁴. The peak position of Fe 2p_{3/2} B-sites and Fe 2p_{1/2} B-sites coincided with the peak positions of Fe²⁺ species²⁵, indicating that Fe²⁺/Fe³⁺ ions could occupy the octahedral sites. The HRXPS Co 2p spectrum (Supplementary Fig. 6(a)) showed two peaks at 782.06 eV and 787.53 eV, which were due to the existence of Co²⁺ ions²⁶. For the HRXPS Ni 2p spectrum (Supplementary Fig. 6(b)), two spin-orbit doublets corresponding to the characteristic peaks of Ni²⁺ (853.61 eV) and Ni³⁺ (855.23 eV) and two shakeup satellites (860.44 eV and 878.19 eV) were observed showing a peculiar existence of Ni³⁺ in the NiF photocatalyst²⁷. Supplementary Figure 6(c) showed the binding energies of Cu 2p_{3/2} (933.90 eV) and Cu 2p_{1/2} (953.76) with two satellites confirming the presence of Cu²⁺ ions in CuF

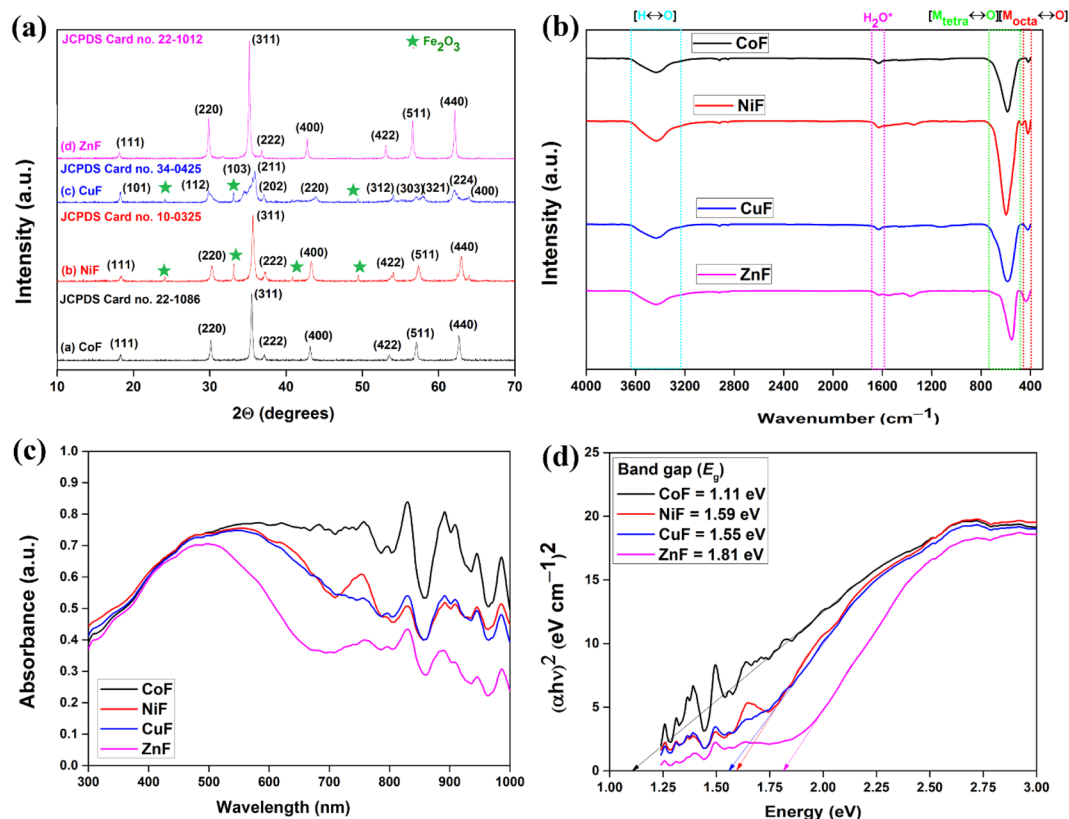


Figure 2. (a) XRD spectra; (b) FTIR spectra; (c) UV-Vis DRS spectra; (d) band gap energies of ferrites photocatalysts.

photocatalyst²⁸. Supplementary Figure 6(d) showed two peaks at 1020.37 eV and 1043.50 eV for Zn^{2+} corresponding to $Zn\ 2p_{3/2}$ and $Zn\ 2p_{1/2}$, respectively for ZnF photocatalyst²⁹.

The electron spin resonance (ESR) spectrum of ZnF photocatalyst has been shown in Supplementary Fig. 7. In ZnF, two systems contribute toward ESR signals: one is high spin Fe^{3+} (d^5) coordinated with oxygen, and the other is singly ionized oxygen vacancy (V_O^+). The doubly ionized (V_O^{+2}) and non-ionized (V_O^0) oxygen vacancies are ESR silent³⁰. The Zn^{2+} ions with filled d^{10} orbital do not contribute to the ESR signal. In the present case, a signal was recorded at $g = 2.001$, which was assigned to V_O^+ . The signal at $g = 2.232$ for Fe^{3+} ion in the octahedral site of spinel ferrite was not observed. The signal was masked by the signal at $g = 2.001$, which could be due to the effect of calcination of ferrite photocatalyst at $700^\circ C$ ³¹.

Photocatalytic activity of ferrites. The photocatalytic activity of all the four ferrites, i.e., CoF, NiF, CuF, and ZnF, was found unsatisfactory in the absence of H_2O_2 and only 30–35% of dye was found to degrade after 60 min of UV irradiation (Fig. 4(a)). Unfortunately, the photogenerated electron-hole pairs were less effective for the process due to fast recombination. In the absence of photocatalyst, less than 8% of dye degradation was observed with H_2O_2 . In the presence of UV and H_2O_2 , nearly 10% decolorization was recorded without any photocatalyst. In the dark condition, nearly 14% of MB dye was adsorbed onto NiF after 5 min of agitation. Thus, it was evident that the contribution of adsorption in photocatalytic degradation of dye would be even lesser due to faster degradation kinetics. The H_2O_2 -assisted photodegradation of organic dye over ferrite photocatalysts showed rapid decolorization at neutral pH. As shown in Fig. 4(b), more than 90% of MB dye was found to degrade within 75 s of irradiation over ferrite photocatalysts. The high-intensity peak at 664 nm is due to conjugation between two dimethylamine substituted aromatic rings through S and N. In contrast, the low-intensity peak in the ultraviolet region (~ 292 nm) appears due to the aromatic rings. From Fig. 4(d), it was evident that along with the fast decolorization of MB dye-containing solution (due to complete breakdown of the chromophore), the intensity of 292 nm peak also decreased with time without forming any new band in the UV or visible region. Thus, it was concluded that complete structural degradation of MB dye was possible in UV-C/ H_2O_2 /ferrite system. The photocatalytic degradation follows the pseudo-first-order kinetic model (Eq. 3) which could be expressed mathematically as³²:

$$\ln\left(\frac{C_t}{C_0}\right) = -k_{app}t \quad (2)$$

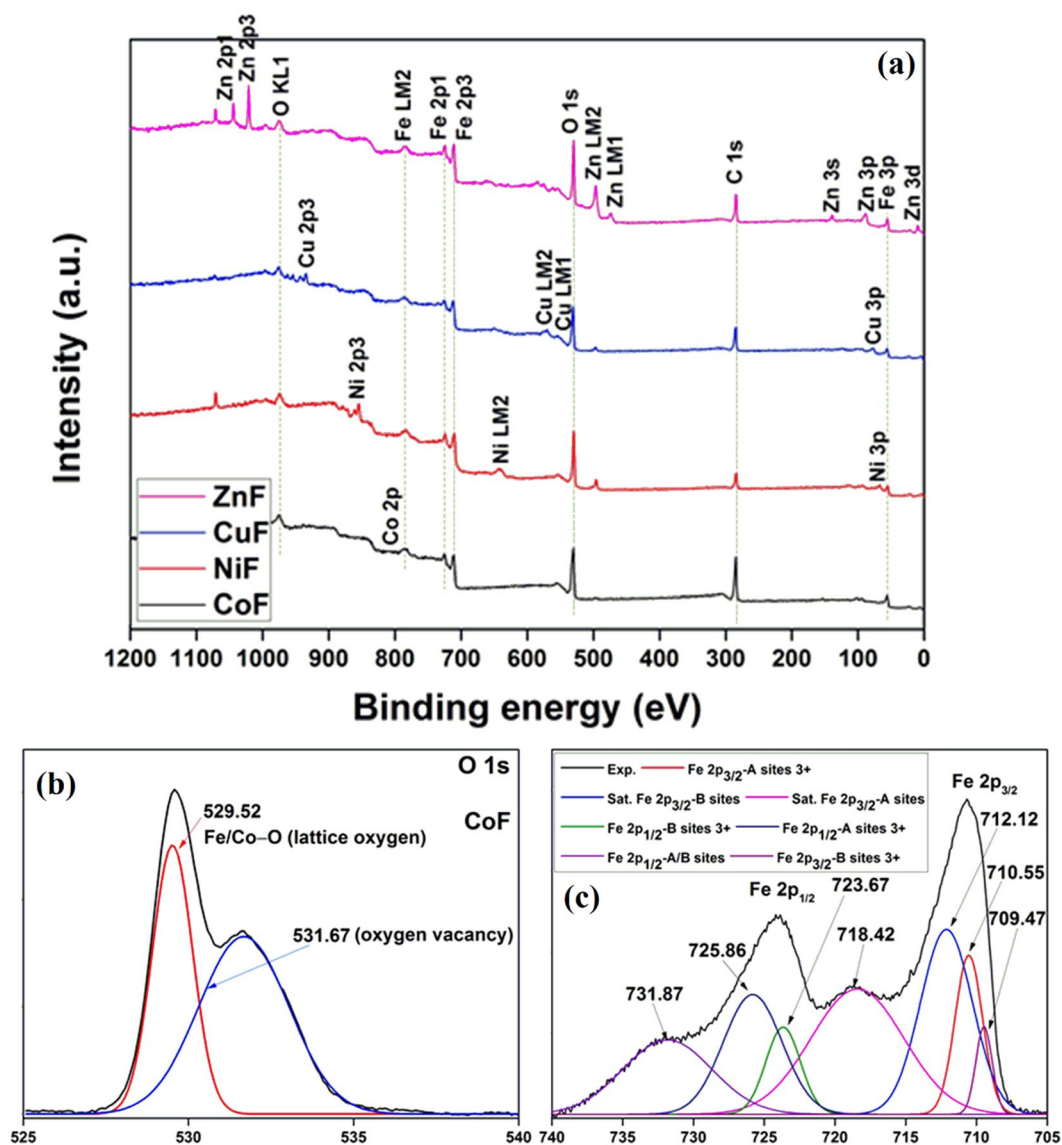


Figure 3. (a) XPS full scan; (b) HRXPS O 1s spectrum (CoF); (c) HRXPS Fe 2p spectrum (CoF).

$$t_{1/2} = \frac{0.693}{k_{app}} \quad (3)$$

where C_0 and C_t are the MB concentration at time $t = 0$ and time ' t ', respectively, and $t_{1/2}$ is the half-life of the dye degradation. The slope of the $\ln(C_t/C_0)$ versus t plot is the apparent rate constant for the reaction (k_{app}). From Fig. 4(c), the calculated k_{app} value was 2.141 min^{-1} , 2.417 min^{-1} , 2.065 min^{-1} , and 2.069 min^{-1} , for CoF, NiF, CuF, and ZnF, respectively. The kinetic rate of degradation for ferrite photocatalysts in this study was found significantly higher than those reported in the literature^{32,33}. The parameters evaluated from the kinetic model, along with the linear regression value, have been displayed in Supplementary Table 3.

Figure 5(a) shows the effect of photocatalyst loading on the MB degradation under the defined experimental conditions for $M\text{Fe}_2\text{O}_4$ ($M = \text{Co}, \text{Ni}, \text{Cu}, \text{Zn}$). Increasing the photocatalyst dosage from 0.05 g L^{-1} to 0.50 g L^{-1} yielded a slight increase in the %dye degradation performance. The increased photocatalyst dosage favored the degradation process by providing more active sites for the generation of active radicals. Moreover, a small dosage of 0.05 g L^{-1} was found enough for ~90% of MB degradation. Since the maximum dye degradation efficiency was recorded for 0.5 g L^{-1} dosage, subsequent experiments were performed with 0.5 g L^{-1} of the photocatalyst.

In the defined experimental conditions, high degradation efficiencies (~92–94%) were recorded for 10–20 mg L^{-1} solution (Fig. 5(b)). Whereas, it dropped to ~65–70% for a 50 mg L^{-1} MB solution. The primary reason for the result obtained was the limited production of active radicals, which were insufficient to degrade the higher concentration of MB dye³⁴. Also, highly concentrated MB dye solution could decrease the penetration of photons in the solution phase and thus hampered with the photogeneration of electron-hole pairs³⁵.

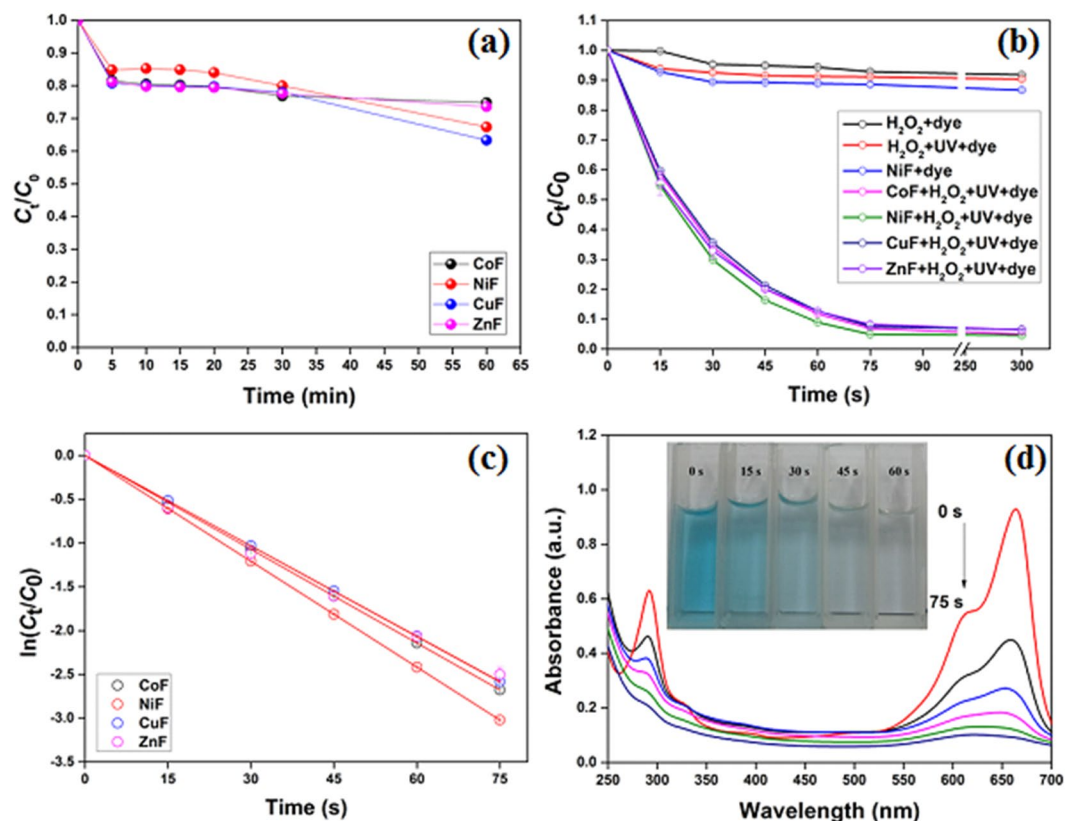


Figure 4. Degradation of MB dye over ferrite photocatalysts. (a) UV irradiation; (b) photocatalytic degradation in H_2O_2/UV system (c) plot of $\ln(C_t/C_0)$ versus time (t); (d) intensity change with irradiation time (ZnF). Conditions: $[MB] = 10 \text{ mg L}^{-1}$, $[\text{photocatalyst}] = 0.5 \text{ g L}^{-1}$, $[H_2O_2] = 5 \text{ mmol L}^{-1}$.

It was observed that with the increase in the H_2O_2 concentration, the MB degradation efficiency decreased by ~3–5% for all the photocatalysts (Fig. 5(c)). In general, an increased H_2O_2 concentration favors the process by providing $\bullet OH$ radicals. Nevertheless, the increased H_2O_2 concentration disfavored the photocatalytic process due to the generation of hydroperoxyl radicals ($HOO\bullet$), which exhibits lower oxidation capabilities and did not contribute to the degradation process¹⁶ (Eqs. 4 and 5). Moreover, radical-radical reactions could have competed with the radical-dye reactions and led to a decreased degradation performance¹⁵ (Eq. 6). Thus, H_2O_2 concentration of 5 mmol L^{-1} was found suitable for the dye degradation process.



For an energy-efficient process, the power required for the dye degradation was optimized by taking the number of 8 W UV lamps into consideration. As shown in Fig. 5(d), more than 90% of the dye was found to degrade under one lamp of 8 W. But with the increase in the number of lamps from two to four, the photocatalytic performance reached up to 95%. An increased UV power led to the adsorption of more photons by the photocatalysts, which in turn accelerated the formation of electron-hole pairs. Considering the power-to-performance ratio, 16 W, i.e., two 8 W lamps, were taken as the illumination source for subsequent studies.

TOC analysis was done to evaluate the mineralization efficiency of a ferrite photocatalyst. The %TOC removal performance of NiF photocatalyst has been shown in Fig. 6(a). In the first 15 s of the degradation process, only 1.1% mineralization of organic species was observed. It increased to 40.0% and 60.2% after 5 min and 50 min, respectively. Thus, it was confirmed that MB dye could be effectively mineralized into residual organic molecules in $UV/H_2O_2/NiF$ system.

The optimized parameters were used for the photocatalytic degradation of methyl orange (MO), bromo green (BG), and methyl red (MR) over NiF photocatalyst. Similar experiments were performed, and the photocatalytic performances have been shown in Fig. 6(b). Within 1 min of the irradiation time, nearly 91.8% of MO, 92.5% of BG, and 77.2% of MR were degraded by NiF photocatalyst, which increased to 94.0% (MO), 93.3% (BG), and 81.8% (MR) after 5 min. Thus, these ferrite photocatalysts in the $UV-C/H_2O_2$ system exhibited remarkable properties for rapid degradation of toxic organic dyes at neutral pH.

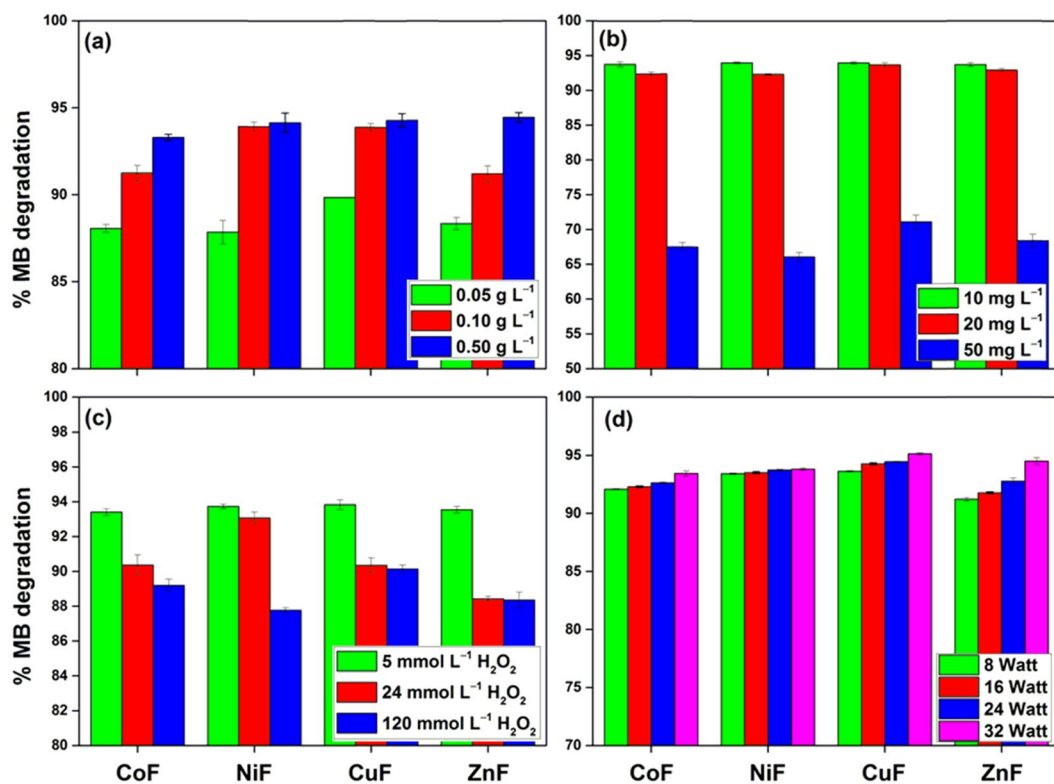


Figure 5. Effect of (a) Photocatalyst dosage; (b) Dye concentration; (c) H₂O₂ concentration; (d) UV-C power on the degradation of MB dye onto ferrite photocatalysts. Conditions: [MB] = 10 mg L⁻¹, [photocatalyst] = 0.5 g L⁻¹, [H₂O₂] = 5 mmol L⁻¹, UV-C power = 16 W, time = 5 min (changed accordingly).

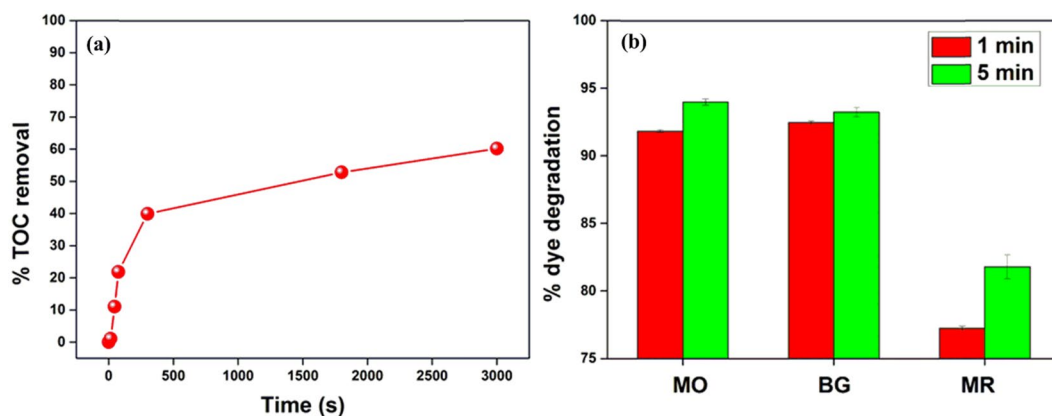


Figure 6. (a) The TOC removal efficiency of MB dye using NiF photocatalyst. (b) Degradation of MO, BG, and MR dyes. Conditions: [Dye] = 10 mg L⁻¹, [H₂O₂] = 5 mmol L⁻¹, [NiF] = 0.5 g L⁻¹, UV-C power = 16 W.

Photocatalytic degradation mechanism. Different scavenging experiments were performed to identify the main active species responsible for the photocatalytic degradation of organic dyes onto ferrite photocatalysts. EDTA, K₂Cr₂O₇, and *p*-benzoquinone were used as a scavenger for the hole (h^+), electron (e^-), and superoxide anion radical ($\cdot O_2^-$), respectively. Tert-butanol was chosen as a hydroxyl radical scavenger for all $\cdot OH$ generated in the reaction process, whereas KI was used as a surface-bound $\cdot OH$ ($\cdot OH_{surf}$) scavenger at the catalytic surface^{36,37}. As evident from Fig. 7(a), the degradation performance decreased in the order: tert-butanol > KI > EDTA > K₂Cr₂O₇ > *p*-benzoquinone > no scavenger. Since the presence of tert-butanol severely affected the photocatalytic process, it was conclusive that the generated $\cdot OH$ radicals were the primary active species for the degradation process. Additionally, the presence of KI lowered the degradation performance by ~40% within 1 min, suggesting that surface-bound ($\cdot OH_{surf}$) released into the solution and took part in the dye degradation process. When ferrite photocatalyst was irradiated under UV lamps, electron/hole (e^-/h^+) pairs were generated on the surface (Eq. 7). The primary pathway for the generation of $\cdot OH$ radicals was the Fenton reaction, where H₂O₂

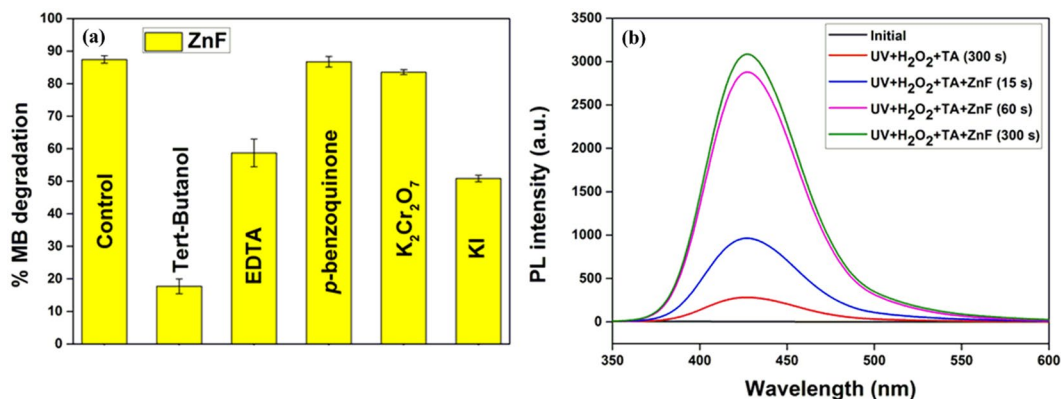
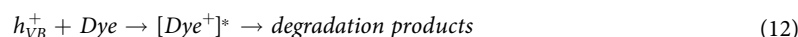
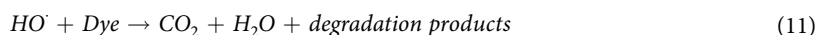
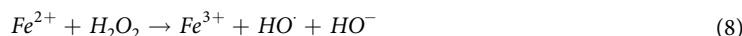


Figure 7. (a) Photocatalytic degradation of MB dye over ZnF photocatalyst in the presence of scavengers; (b) Fluorescence spectra of 2-hydroxy terephthalic acid (TAOH) ($\lambda_{\text{ex}} \sim 315 \text{ nm}$) in the presence of ZnF.

was activated by regenerated Fe^{2+} (Eq. 8). The regeneration of was possible due to the reaction of Fe^{3+} ions with photogenerated e^- ($E^0(\text{Fe}^{3+}/\text{Fe}^{2+}) = +0.77 \text{ V}$) in the conduction band (Eq. 9). The dye degradation performance decreased from ~89% to ~54% in the presence of EDTA, suggesting the involvement of h^+ (photogenerated in the valence band of ZnF) directly in the degradation of MB dye (Eq. 12). The dye degradation process was also affected by the scavenging behavior of $\text{K}_2\text{Cr}_2\text{O}_7$ and *p*-benzoquinone. The photogenerated e^- in the conduction band of ZnF reacted with the adsorbed O_2 molecules to yield $^{\bullet}\text{O}_2^-$ (Eq. 10), which either reacted directly with the MB dye (Eq. 13) or further combined with H^+ to produce $^{\bullet}\text{OH}$ radicals. From the study, it was conclusive that $^{\bullet}\text{OH}$ (Eq. 11) and h^+ served as the major active species, whereas electron was minor active species.



The formation of $^{\bullet}\text{OH}$ radicals on the surface of ZnF photocatalyst in the UV/ H_2O_2 system was further probed by fluorescence spectroscopy using terephthalic acid (TA) as a probe for $^{\bullet}\text{OH}$ radicals. The non-fluorescent TA molecule reacts with an $^{\bullet}\text{OH}$ radical to form fluorescent TAOH. The fluorescent intensity of TAOH is directly proportional to the formation of $^{\bullet}\text{OH}$ radicals in the photocatalytic reaction and is expected to increase with the irradiation time³⁸. When the solution was excited at $\lambda_{\text{ex}} \sim 315 \text{ nm}$, the fluorescence emission was observed at $\lambda_{\text{em}} \sim 425 \text{ nm}$ for TAOH (Fig. 7(b)). Some $^{\bullet}\text{OH}$ radicals were generated by UV irradiation of H_2O_2 via homolytic cleavage, which translated as a low fluorescence emission in the absence of ZnF photocatalyst. In the presence of ZnF, the fluorescence intensity increased with the irradiation time and reached the maximum after 5 min. Thus, it was conclusive that the formation of $^{\bullet}\text{OH}$ radicals primarily drove the photodegradation process. A schematic illustration of the photocatalytic degradation mechanism of MB dye onto ZnF has been shown in Fig. 8.

Effect of anions and reusability. The degradation of MB dye in a photocatalytic process is strongly influenced by the presence of anions such as SO_4^{2-} , NO_3^- , Cl^- , CO_3^{2-} , etc.³⁹. The effect of inorganic anions was evaluated by subjecting MB solution with 100 mg L^{-1} concentration of anions to the photodegradation process. The %MB degradation efficiency was found to be 94.7%, 94.1%, 93.3%, 93.4%, and 94.1% for no anion, NO_3^- , SO_4^{2-} , Cl^- , and CO_3^{2-} , respectively (Fig. 9(a)) showing that anions have an insignificant effect on the dye degradation efficiency of ZnF photocatalyst. The reusability of photocatalysts is required for their practical application on an industrial scale. Here also, the photocatalytic performance of NiF photocatalyst was evaluated for seven cycles by regenerating photocatalyst only by washing and drying at 100°C . In Fig. 9(b), NiF photocatalyst inevitably showed a higher degree of stability and photocatalytic activity towards the degradation of MB dye for seven consecutive runs. Nearly 6.0% loss in photodegradation efficiency was observed after the seventh cycle making these photocatalysts highly suitable for even more cycles.

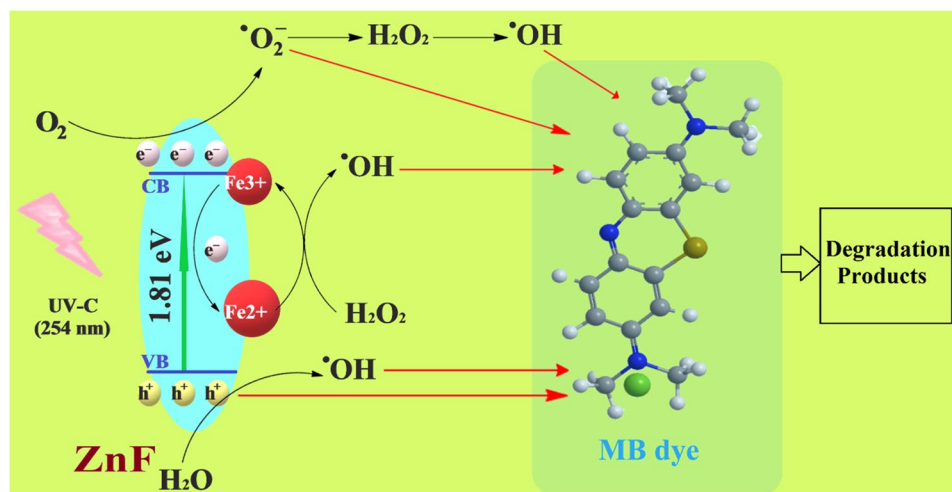


Figure 8. Schematic illustration of photocatalytic degradation process of MB dye onto ZnF photocatalyst.

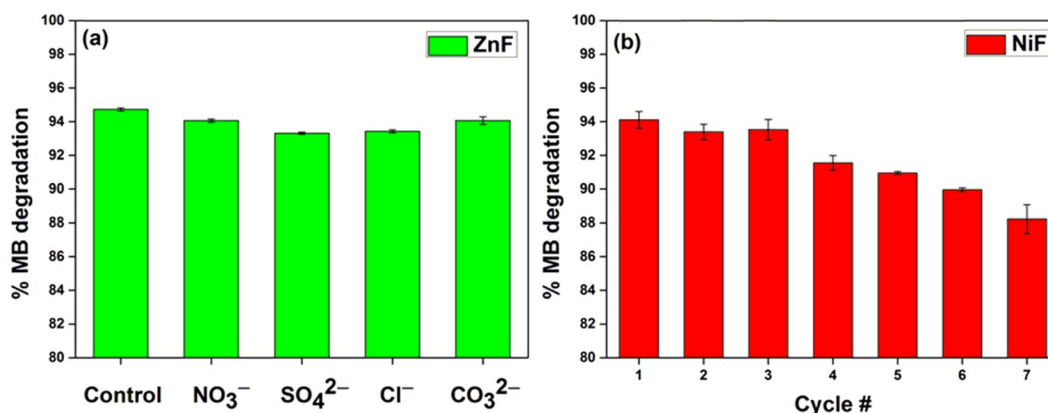


Figure 9. (a) Effect of anions on the degradation of MB dye onto ZnF photocatalyst. Conditions: [MB] = 10 mg L⁻¹, [anion] = 100 mg L⁻¹, [H₂O₂] = 5 mmol L⁻¹, [photocatalyst] = 0.5 g L⁻¹, time = 5 min; (b) Reusability of NiF photocatalyst for seven successive cycles for the degradation of MB.

Conclusions

In this study, we have demonstrated excellent photocatalytic activity of MFe₂O₄ nanoparticles synthesized by the CTAB-mediated co-precipitation-oxidation method. The XRD and TEM analysis confirmed cubic symmetry for CoF, NiF, and ZnF with crystallite size in the range of 27–36 nm. The CuF nanoparticles were in the tetragonal symmetry with 16 nm as the crystallite size. All the ferrites absorbed effectively in the UV-Vis-NIR region. The ferrites were used for the photocatalytic degradation of organic dyes in neutral pH conditions. In optimized experimental conditions, NiF showed an extraordinary rate of 2.417 min⁻¹ for MB dye degradation, which decreased to 2.065 min⁻¹ for ZnF. The NiF photocatalyst showed 89%, 92%, 93%, and 78% decolorization of MB, MO, BG, and MR, respectively, in the same experimental conditions. A 40% TOC removal was observed in the first 5 min of the degradation process, which further increased to 60% after 50 min. The dye degradation mechanism in the UV/H₂O₂/ferrite system was primarily driven by the formation of •OH radicals and holes, which was confirmed by scavenger studies and fluorescence spectroscopy. Apart from being highly reusable, the photocatalyst showed excellent performance in the presence of a ten-fold concentration of salts. From this study, it was concluded that these photocatalysts have the potential to be used for the affordable treatment of dye-contaminated wastewater without modifying the pH under low power UV-C irradiation.

Methods

All the chemicals were of analytical grade and used without any further purification, whose details are available in Supplementary Section 2. MFe₂O₄ NPs were synthesized by the surfactant-mediated co-precipitation method⁴⁰. For the synthesis of CoFe₂O₄, 4.76 g of CoCl₂•6H₂O and 16.16 g of Fe(NO₃)₃•9H₂O were dissolved in 500 mL of distilled water at 60 °C with constant stirring for 10 min. To it, 1.0 g cetyl trimethylammonium bromide was added and vigorously stirred at 60 °C for 30 min. To this solution, 1.0 mol L⁻¹ NaOH solution was added until pH 12 was achieved. After stirring for 1 h, the precipitate was separated, washed with distilled water several times, and dried at 100 °C for 24 h. The dried precipitate was finely grounded before subjecting it to calcination

for 24 h at 700 °C. The same protocol was adopted for the synthesis of NiFe₂O₄, CuFe₂O₄, and ZnFe₂O₄ using 4.75 g of NiCl₂•6H₂O, 4.99 g of CuSO₄•5H₂O, and 5.95 g of Zn(NO₃)₂•6H₂O, respectively along with 16.16 g of Fe(NO₃)₃•9H₂O. As-synthesized ferrites, CoFe₂O₄, NiFe₂O₄, CuFe₂O₄, and ZnFe₂O₄, were abbreviated as CoF, NiF, CuF, and ZnF, respectively.

The synthesized ferrites were characterized by various microscopic and spectroscopic techniques whose details are available in Supplementary Section 3. The photocatalytic performance of synthesized ferrites nanoparticles was evaluated by degrading MB dye in an acryl reactor with four UV lamps (8 W, I_{max} ~254 nm, Philips, The Netherlands) installed in a rectangular assembly. All the experiments were performed at 20 ± 2 °C (temperature was maintained by cooling fans attached at the bottom of the reactor) and at a near-neutral pH condition. For the photodegradation study, 100 mg of a ferrite photocatalyst along with 200 mL of MB solution (10 mg L⁻¹) was taken in a 250 mL pyrex glass tube and subjected to UV-irradiation. After the desired contact time, 5 mL of the aqueous phase was taken out with a disposable syringe filter (Hyundai micro, Model: SN25P045NS) having a microfiltration membrane (pore size: 0.45 μm) to lock the photocatalyst. The locked photocatalyst was pumped back into the aqueous solution by pumping 2 mL of the aqueous phase through the syringe. The remaining 3 mL of the sample solution was analyzed by UV-Vis spectroscopy (LAMBDA 365 UV/Vis Spectrophotometer, Perkin Elmer) after suitable dilution. For photocatalytic degradation process, the same protocol as stated above was followed where 0.1 mL of 28% H₂O₂ solution was added and samples were collected at 15 s, 30 s, 45 s, 60 s, 75 s, and 300 s. Similar protocol was adopted for parameter optimization study of photocatalyst loading, dye concentration, H₂O₂ concentration, and UV power as well as for different dye degradation study. For the detection of active species in the photocatalytic process, 2 mL of scavenger solution (tert-butanol, EDTA, K₂Cr₂O₇, *p*-benzoquinone, or KI) was added into the aqueous phase. The effect of anion on the MB degradation was studied by taking 100 mg L⁻¹ of NO₃⁻, SO₄²⁻, Cl⁻, or CO₃²⁻ anion in the above experiment process. For reusability study, the catalytic efficiency was measured for every cycle using the same protocol where the spent photocatalyst was separated, washed thrice with distilled water, dried in an oven at 100 °C, and used for the next catalytic cycle. The dye degradation efficiency was calculated using Eq. 14.

$$\% \text{ dye degradation} = \left(\frac{C_0 - C_t}{C_0} \right) \times 100 \quad (14)$$

where C₀ and C_t are the initial dye concentration and dye concentration at a time 't', respectively. All the experiments were carried out using three replicate measurements, and the standard deviation associated with data was found to be less than 5%. The data presented in figures are the average of three values, and the bar represents the standard error of the mean value.

Received: 13 November 2019; Accepted: 5 March 2020;

Published online: 18 March 2020

References

- Bharagava, R. N. Recent advances in environmental management. First edition. edn, (2019).
- Mondal, S. Advances in dye removal technologies. (Springer Berlin Heidelberg, 2017).
- Tsuboy, M. S. *et al.* Genotoxic, mutagenic and cytotoxic effects of the commercial dye CI Disperse Blue 291 in the human hepatic cell line HepG2. *Toxicol. In Vitro* **21**, 1650–1655 (2007).
- Chung, K. T. Azo dyes and human health: A review. *J. Environ. Sci. Health. C Environ. Carcinog. Ecotoxicol. Rev.* **34**, 233–261 (2016).
- Das, S., Dash, S. K. & Parida, K. M. Kinetics, isotherm, and thermodynamic study for ultrafast adsorption of azo dye by an efficient sorbent: Ternary Mg/(Al + Fe) layered double hydroxides. *ACS Omega* **3**, 2532–2545 (2018).
- Ojemaye, M. O. & Okoh, A. I. Multiple nitrogen functionalized magnetic nanoparticles as an efficient adsorbent: synthesis, kinetics, isotherm and thermodynamic studies for the removal of rhodamine B from aqueous solution. *Sci. Reports* **9**, 9672 (2019).
- Zhu, M. X., Lee, L., Wang, H. H. & Wang, Z. Removal of an anionic dye by adsorption/precipitation processes using alkaline white mud. *J. Hazard. Mater.* **149**, 735–741 (2007).
- Sen, S. K., Raut, S., Bandyopadhyay, P. & Raut, S. Fungal decolouration and degradation of azo dyes: A review. *Fungal Biol. Rev.* **30**, 112–133 (2016).
- Sharma, A., Ahmad, J. & Flora, S. J. S. Application of advanced oxidation processes and toxicity assessment of transformation products. *Environ. res.* **167**, 223–233 (2018).
- Minella, M. *et al.* Photo-Fenton oxidation of phenol with magnetite as iron source. *Appl. Catal., B* **154–155**, 102–109 (2014).
- Qiang, Z., Chang, J.-H. & Huang, C.-P. Electrochemical regeneration of Fe²⁺ in Fenton oxidation processes. *Water Res.* **37**, 1308–1319 (2003).
- Diya'uddeen Basheer, H., Aziz, A. R. A. & Daud, W. M. A. W. On the limitation of Fenton oxidation operational parameters: A review. *Int. J. Chem. React. Eng.* **10** (2012).
- Garg, V. K., Sharma, V. K. & Kuzmann, E. in Ferrites and Ferrates: Chemistry and applications in sustainable energy and environmental remediation. *ACS Symposium Series*. **5**, 137–143 (2016).
- Pereira, C. *et al.* Superparamagnetic MFe₂O₄ (M = Fe, Co, Mn) nanoparticles: Tuning the particle size and magnetic properties through a novel one-step coprecipitation route. *Chem. Mater.* **24**, 1496–1504 (2012).
- Cai, C. *et al.* Visible light-assisted heterogeneous Fenton with ZnFe₂O₄ for the degradation of Orange II in water. *Appl. Catal., B* **182**, 456–468 (2016).
- Sharma, R., Bansal, S. & Singhal, S. Tailoring the photo-Fenton activity of spinel ferrites (MFe₂O₄) by incorporating different cations (M = Cu, Zn, Ni and Co) in the structure. *RSC Adv.* **5**, 6006–6018 (2015).
- Dhiman, M., Goyal, A., Kumar, V. & Singhal, S. Designing different morphologies of NiFe₂O₄ for tuning of structural, optical and magnetic properties for catalytic advancements. *New J. Chem.* **40**, 10418–10431 (2016).
- Maleki, A., Hajizadeh, Z. & Salehi, P. Mesoporous halloysite nanotubes modified by CuFe₂O₄ spinel ferrite nanoparticles and study of its application as a novel and efficient heterogeneous catalyst in the synthesis of pyrazolopyridine derivatives. *Sci. Reports* **9**, 5552 (2019).
- Hou, H., Xu, G., Tan, S. & Xiang, S. Effects of solvents on the synthesis and infrared radiation emissivity of CuFe₂O₄ spinels. *J. Alloys Compd.* **763**, 736–741 (2018).

20. Balagurov, A. M., Bobrikov, I. A., Pomjakushin, V. Y., Sheptyakov, D. V. & Yushankhai, V. Y. Interplay between structural and magnetic phase transitions in copper ferrite studied with high-resolution neutron diffraction. *J. Magn. Magn. Mater.* **374**, 591–599 (2015).
21. Fareghi-Alamdari, R., Zandi, F. & Keshavarz, M. H. Copper–cobalt synergy in Cu_{1-x}CoxFe₂O₄ spinel ferrite as a highly efficient and regioselective nanocatalyst for the synthesis of 2,4-dinitrotoluene. *RSC Adv.* **5**, 71911–71921 (2015).
22. Yu, C. *et al.* One-pot fabrication of β-Bi₂O₃@ Bi₂S₃ hierarchical hollow spheres with advanced sunlight photocatalytic RhB oxidation and Cr(VI) reduction activities. *Appl. Surf. Sci.* **455**, 8–17 (2018).
23. Wu, L. *et al.* Direct growth of CoFe₂ alloy strongly coupling and oxygen-vacancy-rich CoFe₂O₄ porous hollow nanofibers: an efficient electrocatalyst for oxygen evolution reaction. *Energy Technology* **6**, 2350–2357 (2018).
24. Magno de Lima Alves, T. *et al.* Wasp-waisted behavior in magnetic hysteresis curves of CoFe₂O₄ nanopowder at a low temperature: experimental evidence and theoretical approach. *RSC Adv.* **7**, 22187–22196 (2017).
25. Nandan, R., Gautam, A. & Nanda, K. K. Anthocephalus cadamba shaped FeNi encapsulated carbon nanostructures for metal–air batteries as a resilient bifunctional oxygen electrocatalyst. *J. Mater. Chem. A* **6**, 20411–20420 (2018).
26. Nappini, S. *et al.* Surface Charge and Coating of CoFe₂O₄ Nanoparticles: Evidence of preserved magnetic and electronic properties. *J. Phys. Chem. C* **119**, 25529–25541 (2015).
27. Zheng, X. *et al.* Controllable synthesis of NixSe (0.5 ≤ x ≤ 1) nanocrystals for efficient rechargeable Zinc–Air batteries and water splitting. *ACS Appl. Mater. Interfaces* **10**, 13675–13684 (2018).
28. Dong, S. *et al.* Crystal structure and photocatalytic properties of perovskite MSn(OH)₆ (M = Cu and Zn) composites with d10-d10 configuration. *Appl. Surf. Sci.* **463**, 659–667 (2019).
29. Li, L. *et al.* Uniformly Dispersed ZnFe₂O₄ nanoparticles on Nitrogen-modified graphene for high-performance supercapacitor as electrode. *Sci. Reports* **7**, 43116 (2017).
30. Sarkar, A. & Khan, G. G. The formation and detection techniques of oxygen vacancies in titanium oxide-based nanostructures. *Nanoscale* **11**, 3414–3444 (2019).
31. Li, Y. *et al.* Structural disorder controlled oxygen vacancy and photocatalytic activity of spinel-type minerals: A case study of ZnFe₂O₄. *Chem. Geol.* **504**, 276–287 (2019).
32. Saha, M., Mukherjee, S., Kumar, S., Dey, S. & Gayen, A. Albumin matrix assisted wet chemical synthesis of nanocrystalline MFe₂O₄ (M = Cu, Co and Zn) ferrites for visible light driven degradation of methylene blue by hydrogen peroxide. *RSC Adv.* **6**, 58125–58136 (2016).
33. Wei, F., Wang, H., Ran, W., Liu, T. & Liu, X. Preparation of S–N co-doped CoFe₂O₄@rGO@TiO₂ nanoparticles and their superior UV–Vis light photocatalytic activities. *RSC Adv.* **9**, 6152–6162 (2019).
34. Yu, C. *et al.* Preparation and characterization of sphere-shaped BiVO₄/reduced graphene oxide photocatalyst for an augmented natural sunlight photocatalytic activity. *Journal of Alloys and Compounds* **677**, 219–227 (2016).
35. Parvizi, E. *et al.* Photocatalytic efficacy of supported tetrazine on MgZnO nanoparticles for the heterogeneous photodegradation of methylene blue and ciprofloxacin. *RSC Adv.* **9**, 23818–23831 (2019).
36. Lin, X. H., Miao, Y. & Li, S. F. Y. Location of photocatalytic oxidation processes on anatase titanium dioxide. *Catal. Sci. Technol.* **7**, 441–451 (2017).
37. Dong, S. *et al.* Fabrication of 3D ultra-light graphene aerogel/Bi₂WO₆ composite with excellent photocatalytic performance: A promising photocatalysts for water purification. *J. Taiwan Inst. Chem. Eng.* **97**, 288–296 (2019).
38. Kaviya, S. & Prasad, E. Eco-friendly synthesis of ZnO nanopencils in aqueous medium: a study of photocatalytic degradation of methylene blue under direct sunlight. *RSC Adv.* **6**, 33821–33827 (2016).
39. Bouasla, C., Samar, M. E.-H. & Ismail, F. Degradation of methyl violet 6B dye by the Fenton process. *Desalination* **254**, 35–41 (2010).
40. Gupta, N. K., Ghaffari, Y., Bae, J. & Kim, K. S. Synthesis of coral-like α-Fe₂O₃ nanoparticles for dye degradation at neutral pH. *J. Mol. Liq.*, <https://doi.org/10.1016/j.molliq.2020.112473>. (2020).

Acknowledgements

Authors are grateful for the funds [Project # 20190151–001] provided by the “Korea Institute of Civil Engineering and Building Technology” (KICT), Rep. of Korea.

Author contributions

N.K.G was solely responsible for material synthesis and designing of the experiments. Y.G. and M.S. carried out experiments. N.K.G. and S.K. were responsible for material characterization. J.B. and K.S.K. acquired funds and supervised the work. N.K.G. did the data analysis and prepared the manuscript.

Competing interests

The authors declare no competing interests.

Additional information

Supplementary information is available for this paper at <https://doi.org/10.1038/s41598-020-61930-2>.

Correspondence and requests for materials should be addressed to K.S.K.

Reprints and permissions information is available at www.nature.com/reprints.

Publisher’s note Springer Nature remains neutral with regard to jurisdictional claims in published maps and institutional affiliations.



Open Access This article is licensed under a Creative Commons Attribution 4.0 International License, which permits use, sharing, adaptation, distribution and reproduction in any medium or format, as long as you give appropriate credit to the original author(s) and the source, provide a link to the Creative Commons license, and indicate if changes were made. The images or other third party material in this article are included in the article’s Creative Commons license, unless indicated otherwise in a credit line to the material. If material is not included in the article’s Creative Commons license and your intended use is not permitted by statutory regulation or exceeds the permitted use, you will need to obtain permission directly from the copyright holder. To view a copy of this license, visit <http://creativecommons.org/licenses/by/4.0/>.

© The Author(s) 2020